

# Multi-path Learning for Object Pose Estimation Across Domains

Martin Sundermeyer<sup>1,2</sup>, Maximilian Durner<sup>1,2</sup>, En Yen Puang<sup>1</sup>, Zoltan-Csaba Marton<sup>1</sup>, Rudolph Triebel<sup>1,2</sup>

<sup>1</sup>German Aerospace Center (DLR), <sup>2</sup>Technical University of Munich (TUM)

## Abstract

We introduce a scalable approach for object pose estimation trained on simulated RGB views of multiple 3D models together. We learn an encoding of object views that does not only describe the orientation of all objects seen during training, but can also relate views of untrained objects. Our single-encoder-multi-decoder network is trained using a technique we denote “multi-path learning”: While the encoder is shared by all objects, each decoder only reconstructs views of a single object. Consequently, views of different instances do not need to be separated in the latent space and can share common features. The resulting encoder generalizes well from synthetic to real data and across various instances, categories, model types and datasets. We systematically investigate the learned encodings, their generalization capabilities and iterative refinement strategies on the ModelNet40 and T-LESS dataset. On T-LESS, we achieve state-of-the-art results with our 6D Object Detection pipeline, both in the RGB and depth domain, outperforming learning-free pipelines at much lower runtimes.

## 1. Introduction

Pose estimation, i.e. estimating the 3D rotation and translation, is a cornerstone in many perception related applications (e.g. augmented reality or robotics). For many years this field was dominated by template- and feature-based approaches. Thereby, a given object model (or its features) is matched into the underlying sensor data (e.g. RGB or depth). Depending on the quality of the data and the difficulty of the scene, these approaches can work quite well. In recent years however, machine learning, and in particular Deep Learning (DL) techniques have emerged as another key approach. They often show higher robustness towards sensor noise or environmental changes and can be made computationally efficient. On the other hand, the need of pose-annotated data as well as lengthy training phases make them less flexible compared to traditional methods. To tackle the former, several methods have shifted to train on synthetic data rendered from 3D models [20, 29, 33].

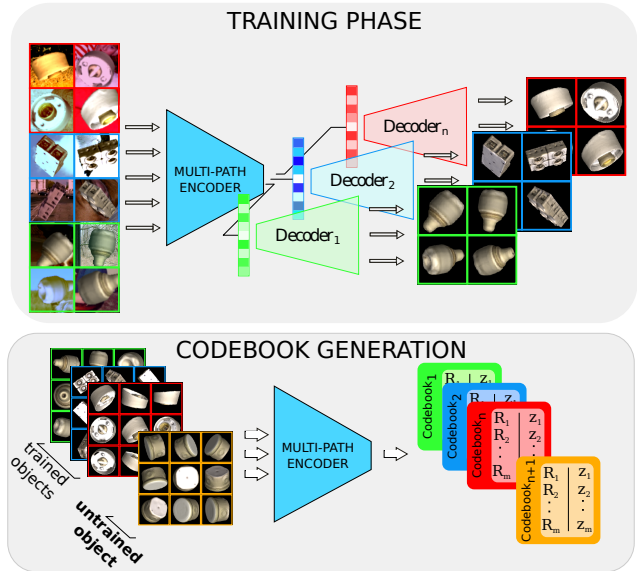


Figure 1: During training a single encoder is shared among all objects, while the decoders reconstruct views of a single object. This turns the encoder into a viewpoint-sensitive feature extractor, that generates expressive encodings for multiple trained and even untrained objects.

However, most of the current learning-based approaches are instance based, meaning they do not generalize well to new instances of the same or different category. In a world with an almost infinite amount of object categories and associated instances the importance of generalization is undeniable. Especially in service robotics we consider the fast adaptation to novel objects a crucial step towards autonomy.

Inspired by the Augmented Autoencoder (AAE) [29] that extracts pose representative features on instance level, we propose a single-encoder-multi-decoder network for estimating the 3D Object Orientation of multiple objects. As we show experimentally, this representation is expressive enough to encode object views that were not seen during training in a view-point sensitive way. These novel instances can originate from known and even unknown categories which can differ significantly from the training domain. We achieve this by sharing one encoder between mul-

multiple decoders which are trained simultaneously with target reconstructions of different shapes (top of Fig. 1). With this multi-path learning strategy, we obtain a *category-agnostic* but shape dependent descriptor of orientation from object views.

These cross-domain encodings are then used in a second step to obtain (relative) orientation estimates, even on untrained objects (bottom of Fig. 1). The proposed single-encoder architecture does not deteriorate the performance compared to separate encoders for each object and even slightly improves encodings of known objects which leads to new state-of-the-art results on T-LESS. Besides that, we introduce an iterative render-inference scheme, which enables the relative pose refinement of untrained objects. We apply this method to iteratively refine poses of untrained instances from ModelNet40 and outperform DeepIM [23], a state-of-the-art approach for RGB-based 6D pose refinement. As a side effect, the iterative refinement can also be used to eliminate discretization errors from codebooks that contain a mapping of latent codes to poses all over  $SO(3)$ , resulting in finer orientation estimates and smaller codebooks.

## 2. Related Work

Object pose estimation has been widely studied in the literature, where existing techniques either use a feature-based approach, or they employ learning techniques.

### 2.1. Feature-/Template-based approaches

Traditionally, pose estimation methods rely on matching algorithms with local keypoints and descriptors or templates. *E.g.*, both Hinterstoisser *et al.* [14] and Vidal *et al.* [35] apply so-called Point Pair Features (PPF) to match a 3D model into a given scene outperforming other results on the SIXD challenge [18] but have runtimes of 4-5 seconds per target due to the exhaustive search in the large 6D pose space. While these methods require depth information, which can be noisy and sensible to environment changes, Ulrich *et al.* [34] use single RGB images and estimate object poses by matching edges of a rendered 3D model into the image. In general, the benefit of such approaches using explicit matching is that no costly training process is required. However, at execution time, these methods tend to require more computational resources. Additionally, usually more expert knowledge is required to set up such pipelines, as feature extraction and matching parameters do not generalize well.

### 2.2. Learning-based Approaches

More recently, a number of learning-based approaches have been presented with the advantage that features are learned implicitly, and that during execution the computation time is reduced. Xiang *et al.* [38] propose a CNN

architecture with multiple stages, where the two pose components are decoupled. The authors also define the pose regression loss as a closest point measure, thus estimations equivalent with respect to an object's shape symmetry are not penalized. In contrast, our proposed approach does not require such an adaptation, because it learns an implicit representation of orientation similar to [29]. *I.e.* it can handle object or view symmetries, which correspond to a one-to-many mapping of object views to poses. These view-centric representations have also been shown to work well for 6D object tracking [6]. Other approaches [36, 12, 20] cope with the problem of symmetries by explicitly adapting the training data. However, this is intractable particularly in case of view-dependent or occlusion-induced symmetries. Rad and Lepetit [28] address this problem by training a convolutional classifier, that predicts symmetries, and processing the input image accordingly. Their so-called BB8 first localizes the object by a coarse segmentation mask, followed by another network inferring the projected 3D bounding box in the 2D image. The pose is then computed by solving the Perspective-n-Point (PnP) problem. Recently, various keypoint-based approaches predicting bounding box corners [32, 9, 33] or inferring semantic keypoints [27] are proposed.

### 2.3. Synthetic training data

One major drawback of learning-based methods is their demand for large amounts of labeled training data. Although there are ways to label object poses semi-automatically [26], it remains a cumbersome process. Recent research tackles this by exploiting synthetic training data. The advantage is that an arbitrary number of data samples with various annotations including pose labels, semantics or segmentation masks can be generated. However, training Convolutional Neural Network (CNN)s with synthetic data usually does not generalize well to real data (reality gap). To bridge this gap, Tremblay *et al.* [33] use mixed training data consisting of *photo-realistic rendering* and *domain randomized* samples. Since photo-realistic renderings are costly, we follow a less expensive Domain Randomization (DR) strategy [20, 32]: 3D models are rendered in poses randomly sampled from  $SO(3)$  and superimposed onto real images from data sets such as MS COCO [24] or Pascal VOC [7].

### 2.4. Generalization to Novel Objects

A further downside of learning-based approaches is that objects used for testing usually need to be from the same domain as the training objects which leads to lengthy training processes on the considered objects. Hence, the idea within this work is to generate category-agnostic pose representative features. CNNs trained on large dataset can be used to extract expressive low-level features for downstream tasks

e.g. image retrieval [10] or classification through clustering. However, applying the naive approach (i.e. extracting feature maps of a network pretrained on ImageNet) to pose related tasks works quite poorly since the low-level features are sensitive to translation while the later layers are semantically unrelated. Additionally, as already mentioned in the last section, features extracted of such a pretrained network strongly differ for synthetic and real object views. Esteves *et al.* [2] propose a cross-domain encoder-decoder to map an object’s 2D image representation into an equivariant feature space of a spherical CNN. The representations are then used to estimate relative poses and novel view synthesis. Although their cross-domain training is only supervised by fixed classification features from a pretrained spherical CNN, they show encouraging results in the task of relative pose estimation. Another work dealing with pose estimation across object instances of a given class is presented in [31]. The so-called KeypointNet learns geometrically and semantically consistent keypoints in an unsupervised manner which are then applied to relative pose estimation. Also, two recent pose refinement methods have been proposed that iteratively predict rotation and translation residuals between an estimated and a target view [25, 23], where the former was shown to generalize to untrained objects of the same category, and the latter even generalizes to objects of new categories. However, these approaches predict an accurate, relative transformation between two object views only in a local neighborhood. In contrast, we aim to retrieve both a global 3D orientation estimate directly and an local, iterative pose refinement across different domains. Another line of work [36, 1] also attempt to directly generate descriptors of an unseen object to predict its orientation and class. Unlike [36, 1], our multi-path training strategy does not separate different object instances in the encoding space and instead allows them to share the same latent features. Our approach differs from category-based pose estimation in that it does not assume fixed, aligned coordinate frames on all instances but rather encodes them according to their appearance. Assigning aligned coordinate frames is often ambiguous in practice because geometries and symmetries of instances within a category can vary a lot. On the contrary, shape and texture primitives are often shared among different categories suggesting that a non-contrastive joint feature extractor would be beneficial.

### 3. Method

We will first briefly describe the AAE (Sec. 3.1). Building upon these results, we then propose a novel Multi-Path Encoder-Decoder architecture and training strategy (Sec. 3.2). Next, we will investigate the encoder on its ability to extract pose-sensitive features and examine generalization to novel instances (Sec. 3.3). Different application scenarios depending on the test conditions are discussed (Sec.

3.4). Finally, an iterative render-inference optimization for pose refinements is presented (Sec. 3.5).

#### 3.1. Implicit Object Pose Representations

Sundermeyer *et al.* [29] have shown that implicit pose representations can be learned in a self-supervised way using an encoder-decoder architecture. This so-called AAE allows to encode 3D orientations from arbitrary object views, generalizes from synthetic training data to various test sensors, and inherently handles symmetric object views.

The AAE is trained to reconstruct rendered views of a single object. To encode 3D orientation exclusively, the inputs are randomly translated and scaled while the reconstruction target stays untouched. To encode object views from real images, the background of input views are randomized, occlusions at various locations are generated, and various lighting and color augmentations are produced. As a result of this *domain randomization*, the network learns to represent the objects’ orientation of real object views implicitly using the latent code  $\mathbf{z}$ .

Concretely, an input sample  $\mathbf{x} \in \mathbb{R}^d$  is randomly augmented by  $f(\cdot)$  and mapped by an encoder  $\Upsilon$  onto a latent code  $\mathbf{z} \in \mathbb{R}^m$  where  $m \ll d$ . The decoder  $\Lambda : \mathbb{R}^m \rightarrow \mathbb{R}^d$  is trained to map the code back to the target  $\mathbf{x}$ .

$$\hat{\mathbf{x}} = \Lambda(\Upsilon(f(\mathbf{x}))) = \Lambda(\Upsilon(x')) = \Lambda(\mathbf{z}) \quad (1)$$

Both  $\Upsilon$  and  $\Lambda$  are neural networks, and their weight parameters are trained such that the  $\ell_2$ -loss is minimized, *i.e.*

$$\ell_2(\mathcal{B}) = \sum_{i \in \mathcal{B}} \|\mathbf{x}_i - \hat{\mathbf{x}}_i\|_2 = \sum_{i \in \mathcal{B}} \|\mathbf{x}_i - \Lambda(\Upsilon(f(\mathbf{x}_i)))\|_2 \quad (2)$$

where  $\mathcal{B}$  contains the indices of input samples of a given batch. After training, the decoder is discarded and latent encodings of object views from all over  $\text{SO}(3)$  are saved in a codebook together with their corresponding orientations assigned. At test time, a real object crop is encoded and the nearest code(s) in the codebook according to cosine similarity yields the predicted orientation.

A downside of this formulation is that a new network must be trained for every new object instance. When naively training the original AAE jointly on several objects, they need to be separated in the latent space so that the decoder is able to reconstruct the correct object. Even when conditioning the decoder on the object by concatenating a one-hot vector to the encoding, it can only reconstruct few instances and diminishes the ability of the encoder to encode object orientations [30].

#### 3.2. Multi-Path Encoder-Decoder

We propose a simple but effective architecture which, in combination with our multi-path learning strategy, enables the 3D orientation estimation of multiple objects (see Fig.

1). Our architecture consists of a single encoder  $\Upsilon$ , an encoding  $\mathbf{z} \in \mathbb{R}^{128}$ , and  $n$  decoders  $\Lambda_j$  with  $j = 1, \dots, n$  where  $n$  is the number of different object shapes (instances). The convolutional encoder is fed with the same augmented inputs as an AAE but with heterogeneous batches  $\tilde{\mathcal{B}}$  containing multiple objects. The resulting codes are split and each decoder only receives codes that correspond to a single object shape. The multi-path loss function can be written as:

$$\begin{aligned} \ell_m(\tilde{\mathcal{B}}) &= \sum_{j=1}^b \sum_{k=1}^n \mathbb{I}(s_j = k) \|\mathbf{x}_j - \Lambda_k(\Upsilon(f(\mathbf{x}_j)))\|_2 \\ &= \sum_{j=1}^b \sum_{k=1}^n \mathbb{I}(s_j = k) \|\mathbf{x}_j - \Lambda_k(\mathbf{z}_j)\|_2 \end{aligned} \quad (3)$$

where  $\mathbb{I}$  is the indicator function used to select the decoder  $\Lambda_k$  that corresponds to the shape index  $s_j$ . Note that in this setting only the encoder  $\Upsilon$  receives information from the entire mini-batch, while the decoders  $\Lambda_j$  backpropagate a loss  $\ell_j$  from a sub-batch. Since the decoders are only used to learn an efficient encoding, they can be discarded after training, leaving behind a compact encoder model.

In contrast to other approaches [36, 1], where objects are explicitly separated in the descriptor space, our encoder can learn an interleaved encoding where general features can be shared across multiple instances. We consider this ability as the main qualification to obtain encodings that can represent object orientations from novel, untrained instances, even when they belong to untrained categories.

### 3.3. Principal Component Analysis of Encodings

In order to gain insights into the characteristics of the latent space from trained and untrained objects, we perform an experiment on the ModelNet40 [37] dataset. We first train the multi-path encoder-decoder on 80 CAD instances that originate from the *car* class. The second model is trained on 10 instances from 8 different classes, namely *airplane*, *bed*, *bench*, *car*, *chair*, *piano*, *sink*, *toilet*. Training details can be found in Sec. 4.2.

After training, we generate 72 viewpoints along a full revolution of azimuth, elevation and in-plane rotation. We record different objects from these viewpoints and feed them into the encoder. From the encoding space  $\mathbf{z}_i \in \mathbb{R}^{128}$  of all objects we compute the first three principal components and project all encodings onto this directions. The interpolated results can be seen in Fig. 2. The top row shows the encodings of a car instance from the training set. The other rows show instances which are not in the training set of neither model, but different sofas and toilets were used to train the second model.

First, it is noticeable that the encodings vary smoothly along each of the rotation axes, even when views of untrained objects are evaluated. It can be seen that the views,

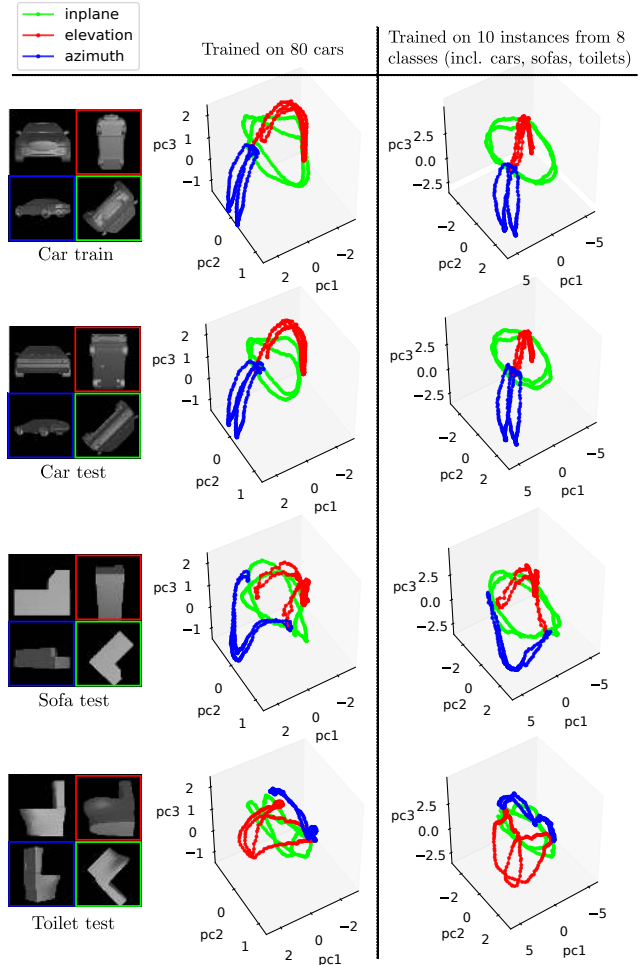


Figure 2: Principal Component Analysis of the learned encodings. Depicted are the encodings of views around elevation (red), azimuth (blue), and in-plane (green). Middle column: Encoder trained only on cars; Right column: Encoder trained on objects from 8 categories

while starting at the same point, end up in different sub-manifolds that capture the shape of the encoded objects and their symmetries. For example, the car instance produces closed trajectories with two revolutions because the car shape looks similar at opposite viewpoints.

Furthermore, it can be seen that the car in the training and test set are encoded similarly by each of the models. This indicates that the encoder as well as the codebook could be reused when predicting orientations of novel cars, without access to their 3D models.

The remaining encodings of untrained objects can still be clearly separated and thus a meaningful pose descriptor could be extracted without retraining the encoder but simply by creating a codebook from their 3D model.

Apart from an offset, both models learn quite similar en-

Table 1: Different application scenarios for global and iterative pose estimation and the handling of untrained objects

| Prerequisites                          | Scenario |    |     |
|--|----------|----|-----|
|  | I        | II | III |
| Category trained                       | ✓        | ✗  | ✓   |
| 3D Test Model available                | ✓        | ✓  | ✗   |
| 3D Test Model aligned to Train Model   | ✓        | ✗  | ✗   |
| Available Methods                      | ↓        | ↓  | ↓   |
| Reuse codebook from a trained instance | ✓        | ✗  | ✓   |
| Create a new full / sparse codebook    | ✓        | ✓  | ✗   |
| Iterative Pose Refinement              | ✓        | ✓  | ✗   |

codings, even for the sofa and toilet category which the first model has not seen during training. This implies that low-level features are extracted that generalize across various shapes and categories. However, to fulfill the reconstruction task the features still need to be robust against lighting and color augmentations as well as translations that are applied to the inputs. In the next section, we will explore different approaches to utilize these properties.

### 3.4. Object Pose Estimation Across Domains

As with the AAE (Sec. 3.1), we can use the trained encoder model and create codebooks, now for all  $n$  training instances and even untrained objects. The single MP-Encoder can exploit batch-wise inference to achieve a runtime that stays almost constant with the number of objects.

An overview of different scenarios when dealing with untrained objects is depicted in Table 1. The trained encoder model is always used as a fixed pose-sensitive feature extractor, but available methods depend on the characteristics and available information of the considered test object.

If no 3D model is available, but we have codebooks of trained instances from the same category, we can reuse these codebooks directly which often yields good pose estimation results. However, we do not explicitly align models of a category in a single coordinate frame, meaning that the extracted representation is more dependent on the shape of an object than on its class.

Therefore, if a test 3D model is available, it is usually preferable to create a new codebook and estimate the pose from it. Finally, we can also use our method for iterative pose refinement at test time. It allows to refine results from sparser codebooks or to do local relative pose estimation without any codebook.

### 3.5. Iterative Refinement of Latent Codes

Our method for iterative pose refinement is outlined below (Alg. 1). We start with an initial pose estimate and a target view. Next, we render a batch of 3D model views at small rotational perturbations from the initial pose and in-

---

#### Algorithm 1: Iterative 6D Pose Refinement

---

**Input:** encoder  $\Upsilon$ , init pose  $\mathbf{q}_{\text{init}}, \mathbf{t}_{\text{init}}$ , target view  $\mathbf{x}_*$   
 $\mathbf{z}_* \leftarrow \Upsilon(\mathbf{x}_*)$   
 $\mathbf{q}_{\text{est}} \leftarrow \mathbf{q}_{\text{init}}$   
 $\mathbf{t}_{\text{est}} \leftarrow \mathbf{t}_{\text{init}}$   
**for**  $k = 0 \dots 2$  **do**  
  **for**  $j = 0 \dots 3$  **do**  
    **for**  $i = 0 \dots 40 - 10k$  **do**  
       $\alpha \sim \mathcal{N}(0, \frac{\sigma^2}{j+1})$   
       $\mathbf{v} \sim \mathcal{N}_3(\mathbf{0}, I)$   
       $\Delta \mathbf{q} \leftarrow \text{quat}(\frac{\mathbf{v}}{\|\mathbf{v}\|}, \alpha)$   
       $\mathbf{q}_i \leftarrow \Delta \mathbf{q} \mathbf{q}_{\text{est}}$   
       $\mathbf{x}_i \leftarrow \text{render}(\mathbf{q}_i, \mathbf{t}_{\text{est}})$   
       $\mathbf{z}_i \leftarrow \Upsilon(\mathbf{x}_i)$   
    **end**  
     $k \leftarrow \arg \max_i \frac{\mathbf{z}_i \cdot \mathbf{z}_*}{\|\mathbf{z}_i\| \|\mathbf{z}_*\|}$   
     $\mathbf{q}_{\text{est}} \leftarrow \mathbf{q}_k$   
  **end**  
   $\mathbf{x}_{\text{est}} = \text{render}(\mathbf{q}_{\text{est}}, \mathbf{t}_{\text{est}})$   
   $\Delta \mathbf{t} = \text{multiScaleEdgeMatching}(\mathbf{x}_*, \mathbf{x}_{\text{est}})$   
   $\mathbf{t}_{\text{est}} = \mathbf{t}_{\text{est}} + \Delta \mathbf{t}$   
**end**  
**Result:**  $\mathbf{q}_{\text{est}}, \mathbf{t}_{\text{est}}$

---

sert the whole batch into the encoder. The code with the highest cosine similarity to the target view encoding determines the new rotation estimate. We sample again with a smaller perturbation radius. The inner loop of this random optimization scheme, consisting of rendering and inference, can be efficiently parallelized.

Rotation and translation are alternately optimized three times. As the MP-Encoder is trained to be invariant against translations, we can first optimize for the difficult out-of-plane rotation offset neglecting translation. Afterwards, the rotation is usually roughly aligned to the target and we can use a simple edge-based, multi-scale template matching method to determine the translation offset. The advantage of sampling in SO(3) vs. sampling in the latent space is that (1) the SO(3) space has lower dimensionality and (2) we only search on the latent manifold that describes valid orientations.

Besides relative pose estimation with a novel 3D model without a codebook, the refinement also allows to trade off between set-up time, inference time, memory resources and accuracy. The full  $92232 \times 128$  codebook creation takes  $\sim 6$  minutes per object on a modern GPU and 45MB space. Inference only takes  $\sim 6$ ms on a modern GPU while the 6D pose refinement in the presented configuration takes approximately 1 second. Depending on the application, i.e. number of objects, available resources and constraints on the set-up time, global initialization with sparse codebooks

Table 2: Comparison of the MP-Encoder performance trained on objects 1-18 on the complete T-LESS primesense test set (RGB-only) compared to 30 single object AAEs [29] trained on all objects. The right column shows the performance of a model trained only on 30 instances of the ModelNet40 dataset. We use the Visible Surface Discrepancy ( $err_{vsd}$ ) metric and ground truth bounding boxes (top) and ground truth masks (bottom) to first gain detector agnostic results.

|          | Mean VSD recall | 30 separate AAE encoders [29] | Single Multi-Path Encoder trained on |                         |
|----------|-----------------|-------------------------------|--------------------------------------|-------------------------|
|          |                 |                               | T-Less Objects 1-18                  | 30 Instances ModelNet40 |
| +gt bbox | Objects 1-18    | 35.6                          | 35.25                                | 27.64                   |
|          | Objects 19-30   | <b>42.45</b>                  | 33.17                                | 34.57                   |
|          | Total           | <b>38.34</b>                  | 34.42                                | 30.41                   |
| +gt mask | Objects 1-18    | 38.98                         | <b>43.17</b>                         | 35.61                   |
|          | Objects 19-30   | <b>45.33</b>                  | 43.33                                | 42.59                   |
|          | Total           | 41.52                         | <b>43.24</b>                         | 38.40                   |

combined with local pose refinement can be a viable option.

### 3.6. 6D Object Detection Pipeline

Our full RGB-based 6D object detection pipeline consists of a MaskRCNN with ResNet50 backbone [11], a projective distance estimate [29] and the MP-Encoder for 3D orientation estimation. To compare against other approaches that use depth data, we also report results with an point-to-plane ICP [4, 39] refinement step. Especially in the presence of severe occlusions the RGB-based projective distance estimate does not produce distances accurate enough to fulfill the strict VSD metric. On the other hand, an accurate initialization is still crucial for ICP refinement. For the MaskRCNN we generate training data by pasting object recordings from the T-LESS training set at random translation, scale and in-plane rotation on random background images. Thereby, we produce 80000 images with Pascal VOC background, 40000 images with black background and 40000 images with random texture backgrounds [5]. We apply several standard online color augmentations like hue, brightness and contrast. Our MaskRCNN reaches a performance of a mAP@0.5 of 0.68 (bbox detection) and 0.67 (segmentation).

## 4. Evaluation

### 4.1. Datasets

We evaluate our approach on the ModelNet40 [37] dataset and the T-LESS dataset [16]. On ModelNet40 we perform RGB-based iterative pose refinement after applying strong 6D pose perturbations. We consider untrained object instances of known and unknown categories to show the generalization properties of the MP-Encoder. Note, that we can train on the unaligned meshes of the original ModelNet40 dataset since our view-based training strategy does not use any pose annotations. To measure the performance on real images, we evaluate our full 6D pose estimation

pipeline on the T-LESS [16] dataset which is a particularly challenging 6D object detection benchmark. Here, we must additionally deal with clutter, occlusions, symmetries and bridge the domain gap between real and synthetic data. We also show results trained on ModelNet but tested on T-LESS.

### 4.2. Architecture and Training Details

We closely follow [29] to design our Multi-Path (MP) encoder and decoders. We have also attempted to adopt the encoder architecture from a state-of-the-art semantic segmentation network, namely DeepLabv3+ [3] but did not find similar performance. This indicates that pose estimation might not require very high level features but rather geometrically accurate ones. All training hyperparameters and architecture details can be found in the appendix.

### 4.3. Metrics

In ModelNet40 we use the absolute angular error

$$e_R = \arccos \left( \text{tr}(\hat{R}^T R - I) / 2 \right) \quad (4)$$

as well as the ADD metric [13] at an average distance threshold of  $0.1 \times$  object diameter for the model points  $\mathcal{M}$

$$ADD = \frac{1}{m} \sum_{x \in \mathcal{M}} \|(Rx + t) - (\hat{R}x + \hat{t})\| \quad (5)$$

and the 2D projection metric at an average 5px threshold

$$Proj2D = \frac{1}{m} \sum_{x \in \mathcal{M}} \|K(Rx + t) - K(\hat{R}x + \hat{t})\| \quad (6)$$

In the T-LESS experiments we use the  $err_{vsd}$  [17] since here the above metrics are quite meaningless as a result of various object and view symmetries. The  $err_{vsd}$  is an ambiguity-invariant pose error metric that is computed from the distance between the estimated and ground truth visible

Table 3: Evaluation of the full 6D Object Detection pipeline with MaskRCNN + Multi-Path Encoder + optional ICP. We report the mean VSD recall following the BOP benchmark [18] on the T-LESS Primesense test set. See appendix for details.

|          | Template matching | PPF based              |                   |                        | Learning-based        |                        |                          |                            |              |
|----------|-------------------|------------------------|-------------------|------------------------|-----------------------|------------------------|--------------------------|----------------------------|--------------|
|          | Hodan-15<br>Depth | Vidal-18<br>Depth +ICP | Drost-10<br>Depth | Drost-10-edge<br>Depth | Brachmann-16<br>RGB-D | Kehl-16<br>RGB-D + ICP | <b>OURS</b><br>RGB + ICP | Sundermeyer-18<br>RGB only | <b>OURS</b>  |
| Average  | 63.18             | 66.51                  | 56.81             | 67.5                   | 17.84                 | 24.6                   | <b>69.53</b>             | 19.26                      | <b>20.53</b> |
| Time (s) | 13.5              | 4.7                    | 2.3               | 21.5                   | 4.4                   | 1.8                    | <b>0.6</b>               | <b>0.1</b>                 | 0.2          |

object surfaces. As in the SIXD challenge 2017 [15] and the BOP benchmark 2018 [19], we report the recall of 6D object poses at  $err_{vsd} < 0.3$  with tolerance  $\tau = 20mm$  and  $> 10\%$  object visibility.

#### 4.4. Generalization Capabilities of the MP-Encoder

We first investigate the joint encoding performance and generalization capabilities of the MP-Encoder. Therefore, we compare one MP-Encoder against 30 separately trained AAE models on all scenes of the T-LESS Primesense test set (Table 2). Equivalent encoder architectures are used. Furthermore, the MP-Encoder is only trained on the first 18 3D object reconstructions of the T-LESS dataset to show the generalization capabilities on untrained objects 19-30. To evaluate the encoding performances for pose estimation in isolation, we use either ground truth detections or masks. On objects 1-18 which the MP-Encoder has seen during training, the results using ground truth bounding boxes are close to the AAE results. Looking at the next row, the performance on the untrained objects 19-30 is significantly worse compared to the single AAEs. We suppose that the MP-Encoder has difficulties to extract unknown objects from the background. This hypothesis is strongly supported by the results with ground truth masks (bottom) where the MP-Encoder even outperforms the AAEs and where the performance gap for the untrained objects 19-30 is much smaller. One possible explanation is that a feature extractor trained on multiple objects learns more expressive features which are more robust. The last column of Table 2 depicts the surprisingly good generalization from ModelNet40 to the T-LESS dataset. Here, the MP-Encoder is specifically trained on 30 texture-free CAD models from the 8 categories *airplane*, *bed*, *bench*, *car*, *chair*, *piano*, *sink*, *toilet*. Codebooks are created for all T-LESS objects and it is tested on the same real sensor recordings. These results underline that with the multi-path training combined with an input randomization strategy, we can learn to extract orientation variant features that generalize well across greatly differing domains.

#### 4.5. 6D Object Detection results

Table 6 presents results with our full 6D object detection pipeline (Sec. 3.6). We achieve state-of-the-art results



Figure 3: Left: Qualitative 6D Object Detection results of the RGB-based pipeline on T-LESS Primesense scenes. Only 18 of 30 objects are used to train the Multi-Path encoder; Middle: ICP-refined results; Right: Relative pose refinement of instances from the untrained categories guitar and bathtub. More results in the appendix.

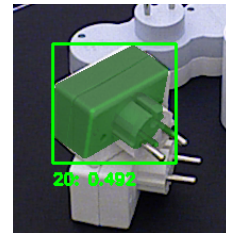


Figure 4: Failure case: MaskRCNN predicts the wrong class 20 instead of 19 (the object below). Since the shape is quite similar (except scale) the codebook of object 20 still gives a reasonable pose estimate.

on T-LESS at much lower runtimes than previous methods, both in the RGB domain and also in the depth domain when initializing an ICP with our RGB-based pose estimate. These results are significant because they show that even for texture-less objects a combination of learning-based pose estimation on RGB and iterative depth-based refinement can reach state-of-the-art results. Particularly, considering that no real pose-annotated data is used for training. Previously, this domain has been dominated by pure geometric matching approaches based on point-pair features that possess very high run-times. They mostly perform 6D Object

Table 4: Relative Pose Refinement from up to  $45^\circ$  and  $\Delta t = (10, 10, 50)[mm]$  perturbations on untrained instances of seen (top) and unseen (bottom) object categories of the ModelNet40 dataset. We measure the recall at the  $5cm, 5^\circ$  threshold, the ADD at 0.1d (object diameter) metric and the Proj2D at 5px threshold.

| metric         | method     | $(5^\circ, 5cm)$ |         |      |             | 6D Pose (ADD) |             |      |             | Proj2D (5px) |             |      |             |
|----------------|------------|------------------|---------|------|-------------|---------------|-------------|------|-------------|--------------|-------------|------|-------------|
|                |            | DeepIm [23]      |         | Ours |             | DeepIm [23]   |             | Ours |             | DeepIm [23]  |             | Ours |             |
|                |            | init             | refined | init | refined     | init          | refined     | init | refined     | init         | refined     | init | refined     |
| novel instance | airplane   | 0.8              | 68.9    | 0.9  | <b>96.9</b> | 25.7          | 94.7        | 33.4 | <b>97.9</b> | 0.4          | 87.3        | 0.1  | <b>97.4</b> |
|                | car        | 1.0              | 81.5    | 0.4  | <b>96.4</b> | 10.8          | 90.7        | 13.4 | <b>98.5</b> | 0.2          | 83.9        | 0.1  | <b>94.0</b> |
|                | chair      | 1.0              | 87.6    | 0.3  | <b>96.4</b> | 14.6          | 97.4        | 16.3 | <b>98.3</b> | 1.5          | 88.6        | 0.0  | <b>94.6</b> |
|                | Mean       | 0.9              | 79.3    | 0.5  | <b>96.6</b> | 17.0          | 94.3        | 21.0 | <b>98.2</b> | 0.7          | 86.6        | 0.1  | <b>95.3</b> |
| novel category | bathtub    | 0.9              | 71.6    | 0.7  | <b>85.5</b> | 11.9          | 88.6        | 15.4 | <b>91.5</b> | 0.2          | 73.4        | 0.1  | <b>80.6</b> |
|                | bookshelf  | 1.2              | 39.2    | 0.7  | <b>81.9</b> | 9.2           | 76.4        | 13.7 | <b>85.1</b> | 0.1          | 51.3        | 0.0  | <b>76.3</b> |
|                | guitar     | 1.2              | 50.4    | 0.5  | <b>69.2</b> | 9.6           | 69.6        | 13.1 | <b>80.5</b> | 0.2          | 77.1        | 0.3  | <b>80.1</b> |
|                | range_hood | 1.0              | 69.8    | 0.5  | <b>91.0</b> | 11.2          | 89.6        | 14.1 | <b>95.0</b> | 0.0          | 70.6        | 0.0  | <b>83.9</b> |
|                | sofa       | 1.2              | 82.7    | 0.6  | <b>91.3</b> | 9.0           | 89.5        | 12.2 | <b>95.8</b> | 0.1          | <b>94.2</b> | 0.0  | 86.5        |
|                | wardrobe   | 1.4              | 62.7    | 0.7  | <b>88.7</b> | 12.5          | 79.4        | 14.8 | <b>92.1</b> | 0.2          | 70.0        | 0.0  | <b>81.1</b> |
|                | tv_stand   | 1.2              | 73.6    | 0.6  | <b>85.9</b> | 8.8           | <b>92.1</b> | 10.5 | 90.9        | 0.2          | 76.6        | 0.1  | <b>82.5</b> |
|                | Mean       | 1.2              | 64.3    | 0.6  | <b>84.8</b> | 10.3          | 83.6        | 13.4 | <b>90.1</b> | 0.1          | 73.3        | 0.1  | <b>81.6</b> |

Localization in contrast to 6D Object Detection and thus do not scale well with the number of considered objects.

Fig. 3 shows qualitative examples of the full pipeline. Fig. 4 shows a failure case. It also shows that strict instance-wise pose estimation may not be suitable for real world applications where objects often differ only in details.

#### 4.6. Iterative Refinement on Untrained Objects

In our final experiment, we evaluate the MP-Encoder on the task of iterative refinement of poses on untrained instances from seen and unseen categories from ModelNet40.

We follow the evaluation protocol of DeepIm [23] where the relative pose between two object views of an untrained instance is sought. The first view is rendered at constant translation  $t = (0, 0, 500)$  (mm) and random rotation  $R \sim SO(3)$ . Then we render another object view with that pose perturbed by an angle  $\beta_{x/y/z} \sim \mathcal{N}(0, (15^\circ)^2)$  sampled for each rotation axis and a translational offset  $\Delta x \sim \mathcal{N}(0, 10^2)$ ,  $\Delta y \sim \mathcal{N}(0, 10^2)$ ,  $\Delta z \sim \mathcal{N}(0, 50^2)$  (mm). If the total angular perturbation is more than  $45^\circ$ , it is resampled.

We train category specific MP-Encoders on 80 instances of the airplane, car and chair class and predict the relative pose on novel instances. We also train a MP-Encoder on 80 instances from 8 different categories<sup>1</sup> to obtain a general viewpoint-sensitive feature extractor which we test on instances from novel categories. To retain the relative pose to the target view we use our random optimization scheme described in Alg. 1 with an initial  $\sigma = 45^\circ$ . We compare

our approach against DeepIm [23] that also minimizes the relative pose between an initial and a target view through an iterative rendering inference cycle. The results in table 4 demonstrate superior performance of our approach on both, seen and unseen categories. Figure 3 on the right shows some qualitative results.

## 5. Conclusion

The ability of our pose estimator to generalize across objects from different categories, datasets and image domains indicates that pose-sensitive features are shared among different instances. These primitive structural and textural features can be extracted and related by a single encoder that is trained using multiple object-specific decoders.

In contrast to other learning-based pose estimation methods, we can (1) use a single model for a large number of different objects, (2) iteratively refine the poses up to very high accuracy and (3) reach state-of-the-art results on the texture-less, symmetric objects of the T-LESS dataset. We believe that this is a step forward in coping with the large number of instances in industrial settings where 3D models are often available and service robotics where categories often appear repeatedly and interactions with novel objects should be immediately possible.

In future, we want to explore how the Multi-Path training paradigm can be translated to other applications in which an interleaved descriptor space over multiple instances is beneficial.

<sup>1</sup>airplane, bed, bench, car, chair, piano, sink, toilet

## References

- [1] Vassileios Balntas, Andreas Doumanoglou, Caner Sahin, Juil Sock, Rigas Kouskouridas, and Tae-Kyun Kim. Pose Guided RGB-D Feature Learning for 3D Object Pose Estimation. In *Proceedings of the IEEE Conference on Computer Vision and Pattern Recognition*, pages 3856–3864, 2017. 3, 4
- [2] Esteves Carlos, Sud Avneesh, Luo Zhengyi, Daniilidis Kostas, and Makadia Ameesh. Cross-domain 3d equivariant image embeddings. *arXiv preprint arXiv:1812.02716*, 2018. 3
- [3] Liang-Chieh Chen, Yukun Zhu, George Papandreou, Florian Schroff, and Hartwig Adam. Encoder-decoder with atrous separable convolution for semantic image segmentation. In *Proceedings of the European Conference on Computer Vision (ECCV)*, pages 801–818, 2018. 6, 10
- [4] Yang Chen and Gérard Medioni. Object modelling by registration of multiple range images. *Image and vision computing*, 10(3):145–155, 1992. 6, 11
- [5] M. Cimpoi, S. Maji, I. Kokkinos, S. Mohamed, , and A. Vedaldi. Describing textures in the wild. In *Proceedings of the IEEE Conf. on Computer Vision and Pattern Recognition (CVPR)*, 2014. 6
- [6] Xinke Deng, Arsalan Mousavian, Yu Xiang, Fei Xia, Timothy Bretl, and Dieter Fox. Poserbpf: A rao-blackwellized particle filter for 6d object pose tracking. *Robotics: Science and Systems (RSS)*, 2019. 2
- [7] Mark Everingham, Luc Van Gool, Christopher KI Williams, John Winn, and Andrew Zisserman. The pascal visual object classes (voc) challenge. *International journal of computer vision*, 88(2):303–338, 2010. 2
- [8] M. Everingham, L. Van Gool, C. K. I. Williams, J. Winn, and A. Zisserman. The PASCAL Visual Object Classes Challenge 2012 (VOC2012) Results. <http://www.pascal-network.org/challenges/VOC/voc2012/workshop/index.html>, 2012. 11
- [9] Alexander Grabner, Peter M. Roth, and Vincent Lepetit. 3d pose estimation and 3d model retrieval for objects in the wild. In *The IEEE Conference on Computer Vision and Pattern Recognition (CVPR)*, June 2018. 2
- [10] Jiedong Hao, Jing Dong, Wei Wang, and Tieniu Tan. What is the best practice for cnns applied to visual instance retrieval? *arXiv preprint arXiv:1611.01640*, 2016. 3
- [11] Kaiming He, Georgia Gkioxari, Piotr Dollár, and Ross Girshick. Mask r-cnn. *arXiv preprint arXiv:1703.06870*, 2017. 6
- [12] Stefan Hinterstoisser, Cedric Cagniard, Slobodan Ilic, Peter Sturm, Nassir Navab, Pascal Fua, and Vincent Lepetit. Gradient response maps for real-time detection of textureless objects. *IEEE Transactions on Pattern Analysis and Machine Intelligence*, 34(5):876–888, 2012. 2
- [13] Stefan Hinterstoisser, Vincent Lepetit, Slobodan Ilic, Stefan Holzer, Gary Bradski, Kurt Konolige, and Nassir Navab. Model based training, detection and pose estimation of texture-less 3D objects in heavily cluttered scenes. In *Asian conference on computer vision*, pages 548–562. Springer, 2012. 6
- [14] Stefan Hinterstoisser, Vincent Lepetit, Naresh Rajkumar, and Kurt Konolige. Going further with Point Pair Features. In *European Conference on Computer Vision*, pages 834–848. Springer, 2016. 2
- [15] Tomas Hodan. SIXD Challenge 2017, [http://cmp.felk.cvut.cz/sixd/challenge\\_2017/](http://cmp.felk.cvut.cz/sixd/challenge_2017/), 2017. 7
- [16] Tomáš Hodaň, Pavel Haluza, Štěpán Obdržálek, Jiří Matas, Manolis Lourakis, and Xenophon Zabulis. T-LESS: An RGB-D Dataset for 6D Pose Estimation of Texture-less Objects. *IEEE Winter Conference on Applications of Computer Vision (WACV)*, 2017. 6
- [17] Tomáš Hodaň, Jiří Matas, and Štěpán Obdržálek. On evaluation of 6D object pose estimation. In *European Conference on Computer Vision*, pages 606–619. Springer, 2016. 6
- [18] Tomas Hodan, Frank Michel, Eric Brachmann, Wadim Kehl, Anders GlentBuch, Dirk Kraft, Bertram Drost, Joel Vidal, Stephan Ihrke, Xenophon Zabulis, et al. Bop: benchmark for 6d object pose estimation. In *Proceedings of the European Conference on Computer Vision (ECCV)*, pages 19–34, 2018. 2, 7, 12, 13
- [19] Tomas Hodan, Frank Michel, Eric Brachmann, Wadim Kehl, Anders GlentBuch, Dirk Kraft, Bertram Drost, Joel Vidal, Stephan Ihrke, Xenophon Zabulis, Caner Sahin, Fabian Manhardt, Federico Tombari, Tae-Kyun Kim, Jiri Matas, and Carsten Rother. Bop: Benchmark for 6d object pose estimation. In *The European Conference on Computer Vision (ECCV)*, September 2018. 7
- [20] Wadim Kehl, Fabian Manhardt, Federico Tombari, Slobodan Ilic, and Nassir Navab. SSD-6D: Making RGB-Based 3D Detection and 6D Pose Estimation Great Again. In *Proceedings of the IEEE Conference on Computer Vision and Pattern Recognition*, pages 1521–1529, 2017. 1, 2
- [21] A. Kendall, M. Grimes, and R. Cipolla. Posenet: A convolutional network for real-time 6-dof camera relocalization. In *2015 IEEE International Conference on Computer Vision (ICCV)*, pages 2938–2946, Dec 2015.
- [22] Diederik Kingma and Jimmy Ba. Adam: A method for stochastic optimization. *arXiv preprint arXiv:1412.6980*, 2014. 11
- [23] Yi Li, Gu Wang, Xiangyang Ji, Yu Xiang, and Dieter Fox. Deepim: Deep iterative matching for 6d pose estimation. *arXiv preprint arXiv:1804.00175*, 2018. 2, 3, 8
- [24] Tsung-Yi Lin, Michael Maire, Serge Belongie, James Hays, Pietro Perona, Deva Ramanan, Piotr Dollár, and C Lawrence Zitnick. Microsoft coco: Common objects in context. In *European conference on computer vision*, pages 740–755. Springer, 2014. 2
- [25] Fabian Manhardt, Wadim Kehl, Nassir Navab, and Federico Tombari. Deep model-based 6d pose refinement in rgb. In *The European Conference on Computer Vision (ECCV)*, September 2018. 3
- [26] Pat Marion, Peter R Florence, Lucas Manuelli, and Russ Tedrake. Label fusion: A pipeline for generating ground truth labels for real rgbd data of cluttered scenes. In *2018 IEEE International Conference on Robotics and Automation (ICRA)*, pages 3325–3242. IEEE, 2018. 2
- [27] Georgios Pavlakos, Xiaowei Zhou, Aaron Chan, Konstantinos G Derpanis, and Kostas Daniilidis. 6-dof object pose

from semantic keypoints. In *International Conference on Robotics and Automation (ICRA)*, 2017. 2

- [28] Mahdi Rad and Vincent Lepetit. BB8: A scalable, accurate, robust to partial occlusion method for predicting the 3D poses of challenging objects without using depth. In *IEEE International Conference on Computer Vision (ICCV)*, 2017. 2
- [29] Martin Sundermeyer, Zoltan-Csaba Marton, Maximilian Durner, Manuel Brucker, and Rudolph Triebel. Implicit 3d orientation learning for 6d object detection from rgb images. In *Proceedings of the European Conference on Computer Vision (ECCV)*, pages 699–715, 2018. 1, 2, 3, 6, 10
- [30] Martin Sundermeyer, En Yen Puang, Zoltan-Csaba Marton, Maximilian Durner, and Rudolph Triebel. Learning implicit representations of 3d object orientations from rgb. In *ICRA Workshop on Representing a Complex World*, 2018. 3
- [31] Supasorn Suwajanakorn, Noah Snavely, Jonathan J Tompson, and Mohammad Norouzi. Discovery of latent 3d keypoints via end-to-end geometric reasoning. In S. Bengio, H. Wallach, H. Larochelle, K. Grauman, N. Cesa-Bianchi, and R. Garnett, editors, *Advances in Neural Information Processing Systems 31*, pages 2059–2070. Curran Associates, Inc., 2018. 3
- [32] Bugra Tekin, Sudipta N. Sinha, and Pascal Fua. Real-Time Seamless Single Shot 6D Object Pose Prediction. In *CVPR*, 2018. 2
- [33] Jonathan Tremblay, Thang To, Balakumar Sundaralingam, Yu Xiang, Dieter Fox, and Stan Birchfield. Deep object pose estimation for semantic robotic grasping of household objects. In *Conference on Robot Learning*, pages 306–316, 2018. 1, 2
- [34] Markus Ulrich, Christian Wiedemann, and Carsten Steger. CAD-based recognition of 3D objects in monocular images. In *ICRA*, volume 9, pages 1191–1198, 2009. 2
- [35] Joel Vidal, Chyi-Yeu Lin, and Robert Martí. 6D Pose Estimation using an Improved Method based on Point Pair Features. *arXiv preprint arXiv:1802.08516*, 2018. 2
- [36] Paul Wohlhart and Vincent Lepetit. Learning descriptors for object recognition and 3D pose estimation. In *Proceedings of the IEEE Conference on Computer Vision and Pattern Recognition*, pages 3109–3118, 2015. 2, 3, 4
- [37] Zhirong Wu, Shuran Song, Aditya Khosla, Fisher Yu, Linguang Zhang, Xiaoou Tang, and Jianxiong Xiao. 3d shapenets: A deep representation for volumetric shapes. In *Proceedings of the IEEE conference on computer vision and pattern recognition*, pages 1912–1920, 2015. 4, 6
- [38] Yu Xiang, Tanner Schmidt, Venkatraman Narayanan, and Dieter Fox. Posecnn: A convolutional neural network for 6d object pose estimation in cluttered scenes. *arXiv preprint arXiv:1711.00199*, 2017. 2
- [39] Zhengyou Zhang. Iterative point matching for registration of free-form curves and surfaces. *International journal of computer vision*, 13(2):119–152, 1994. 6, 11

## A. Appendix

In the following we provide implementation details and show qualitative results. The code will be open sourced upon publication to allow the community to reproduce results.

### A.1. Architecture

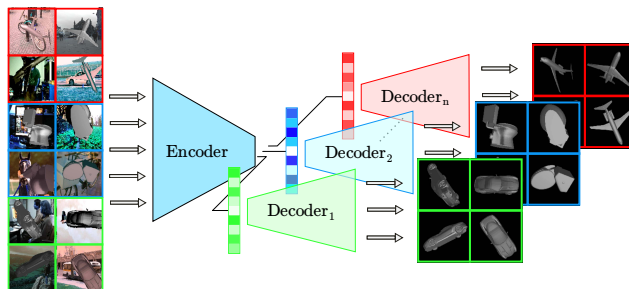


Figure 5: Our multi-path training process. **Left:** Joint augmented input batch with uniformly sampled  $SO(3)$  views of  $n$  object instances; **Right:** Individual reconstruction targets  $x_j$  for each decoder.

In our T-LESS experiments the encoder is symmetric to each of the decoders. The encoder consists of four convolutional layers with kernel size = 5, stride=2, ReLU activation and  $\{128, 256, 512, 512\}$  filters respectively. It follows, a shared fully connected layer with  $W_0 \in \mathcal{R}^{32768 \times 128}$ . The resulting codes are propagated to the corresponding decoders via  $j \in 1, \dots, n$  fully connected layers  $W_j \in \mathcal{R}^{128 \times 32768}$ . After reshaping, each decoder has four consecutive convolutional layers with kernel size = 5, stride=1, ReLU activation and  $\{512, 512, 256, 128\}$  filters. Nearest neighbor upsampling is performed after each convolutional layer. The final reconstruction output is preceded by a sigmoid activation.

We initially expected that an encoder with up to hundred corresponding decoders would require a much larger architecture to be able to adequately encode the views of all training objects. Therefore, we first adopted the [3], with a Resnet101 backbone and a spatial pyramid pooling (SPP) layer. Although, the total training loss can be reduced with such a network, the downstream performance on encoding object poses of both, trained and untrained objects, does not increase compared to a more shallow encoder/decoder with 4-5 plain convolutional layers as used by [29]. As usual, multiple explanations are plausible. The lost symmetry in the encoder-decoder architecture could make an invertible compression more difficult to learn. A deeper encoder could simply overfit more and generalize less. More shallow features contain all necessary low-level information for class-agnostic pose estimation. As architecture search and explanation is not our main goal here, we simply stick with the

more efficient shallow CNN.

## A.2. Training

It is possible to train our architecture with up to 80 decoders on a single GPU. In this case, the encoder receives a joint batch size of 80, while each decoder has a batch size = 1. For single-GPU training on T-LESS with 18 decoders, we use a batch size = 4. We train for 300.000 iterations which takes about 48 hours on a single GPU. Multiple GPUs almost linearly speed up training due to the inherent parallelism in the architecture. Therefore, the batch and the decoders are divided into equal parts on all available GPUs.

We use Xavier initialization and the Adam [22] optimizer with a learning rate of  $10^{-4} \times b_{dec}$ , with  $b_{dec}$  = decoder batch size. In our experiments we did not have to assign individual learning rates to the encoder and decoder but this could potentially accelerate the training.

## A.3. Synthetic Data Generation

For each instance we render 8000 object views sampled randomly from  $SO(3)$  at a constant distance of 700mm. The resulting images are quadratically cropped and resized to  $128 \times 128 \times 3$ .

## A.4. Augmentation Parameters

All geometric and color input augmentations besides the random lighting are applied online during training at uniform random strength (see Table 5). As background images we use Pascal VOC2012 [8]. One could argue that random background images during training are redundant where we use MaskRCNN. But in our experiments it does help with the generalization from synthetic to real data and is also beneficial when the MaskRCNN does not output perfect masks.

Table 5: Augmentation Parameters; Scale and translation is in relation to image shape

| color         | 50% chance<br>(30% per channel)     | light (random position)<br>& geometric |                            |
|---------------|-------------------------------------|--|----------------------------|
| add           | $\mathcal{U}(-0.1, 0.1)$            | ambient                                | 0.4                        |
| contrast      | $\mathcal{U}(0.4, 2.3)$             | diffuse                                | $\mathcal{U}(0.7, 0.9)$    |
| multiply      | $\mathcal{U}(0.6, 1.4)$             | specular                               | $\mathcal{U}(0.2, 0.4)$    |
| invert        |                                     | scale                                  | $\mathcal{U}(0.8, 1.2)$    |
| gaussian blur | $\sigma \sim \mathcal{U}(0.0, 1.2)$ | translation                            | $\mathcal{U}(-0.15, 0.15)$ |

## A.5. ICP Refinement

Optionally, the estimate is refined on depth data using a point-to-plane Iterative Closest Point (ICP) approach with adaptive thresholding of correspondences based on [4, 39]. The refinement is first applied in direction of the vector pointing from camera to the object where most of the RGB-

based pose estimation errors stem from and then on the full 6D pose.

## A.6. Full T-LESS results

Table 6 shows the full T-LESS results on each object tested on all scene views of the Primesense test set. Figure 6 show qualitative results with and without refinement on different T-LESS test scenes.

## A.7. Runtime

The MaskRCNN with ResNet50 takes  $\sim 150ms$  for all instances in a scene on a modern GPU. Lighter architectures can be chosen for simpler problems. All resulting image crops can be batched together such that the inference of the MP-Encoder is parallelized. For a single instance the inference takes  $\sim 5ms$ , nearest neighbor search in the codebook takes  $1 - 2ms$  and the projective distance estimation is negligible. While our RGB-based pipeline runs at high speed and makes our approach applicable for mobile applications, the depth-based ICP refinement takes in average  $0.4s$  per target and is thus suitable for robotic manipulation tasks.

Table 6: Evaluation of the full 6D Object Detection pipeline with MaskRCNN + Multi-Path Encoder + optional ICP. We report the mean VSD recall following the BOP benchmark [18] on the T-LESS Primesense test set.

| object   | Template matching | PPF based              |                   |                        | Learning-based         |                          |                       |                       |              |
|----------|-------------------|------------------------|-------------------|------------------------|------------------------|--------------------------|-----------------------|-----------------------|--------------|
|          | Hodan-15<br>Depth | Vidal-18<br>Depth +ICP | Drost-10<br>Depth | Drost-10-edge<br>Depth | Kehl-16<br>RGB-D + ICP | <b>OURS</b><br>RGB + ICP | Brachmann-16<br>RGB-D | Sundermeyer-18<br>RGB | <b>OURS</b>  |
| 1        | 66                | 43                     | 34                | 53                     | 7                      | 73.61                    | 8                     | 9.48                  | 5.56         |
| 2        | 67                | 46                     | 46                | 44                     | 10                     | 66.40                    | 10                    | 13.24                 | 10.22        |
| 3        | 72                | 68                     | 63                | 61                     | 18                     | 87.24                    | 21                    | 12.78                 | 14.74        |
| 4        | 72                | 65                     | 63                | 67                     | 24                     | 82.91                    | 4                     | 6.66                  | 6.23         |
| 5        | 61                | 69                     | 68                | 71                     | 23                     | 86.16                    | 46                    | 36.19                 | 37.53        |
| 6        | 60                | 71                     | 64                | 73                     | 10                     | 92.79                    | 19                    | 20.64                 | 30.36        |
| 7        | 52                | 76                     | 54                | 75                     | 0                      | 80.83                    | 52                    | 17.41                 | 14.62        |
| 8        | 61                | 76                     | 48                | 89                     | 2                      | 81.32                    | 22                    | 21.72                 | 10.73        |
| 9        | 86                | 92                     | 59                | 92                     | 11                     | 85.15                    | 12                    | 39.98                 | 19.43        |
| 10       | 72                | 69                     | 54                | 72                     | 17                     | 82.31                    | 7                     | 13.37                 | 32.75        |
| 11       | 56                | 68                     | 51                | 64                     | 5                      | 72.60                    | 3                     | 7.78                  | 20.34        |
| 12       | 55                | 84                     | 69                | 81                     | 1                      | 68.80                    | 3                     | 9.54                  | 29.53        |
| 13       | 54                | 55                     | 43                | 53                     | 0                      | 53.37                    | 0                     | 4.56                  | 12.41        |
| 14       | 21                | 47                     | 45                | 46                     | 9                      | 50.54                    | 0                     | 5.36                  | 21.30        |
| 15       | 59                | 54                     | 53                | 55                     | 12                     | 45.25                    | 0                     | 27.11                 | 20.82        |
| 16       | 81                | 85                     | 80                | 85                     | 56                     | 82.32                    | 5                     | 22.04                 | 33.20        |
| 17       | 81                | 82                     | 79                | 88                     | 52                     | 72.27                    | 3                     | 66.33                 | 39.88        |
| 18       | 79                | 79                     | 68                | 78                     | 22                     | 80.60                    | 54                    | 14.91                 | 14.16        |
| 19       | 59                | 57                     | 53                | 55                     | 35                     | 48.17                    | 38                    | 23.03                 | 9.24         |
| 20       | 27                | 43                     | 35                | 47                     | 5                      | 25.74                    | 1                     | 5.35                  | 1.72         |
| 21       | 57                | 62                     | 60                | 55                     | 26                     | 47.53                    | 39                    | 19.82                 | 11.48        |
| 22       | 50                | 69                     | 61                | 56                     | 27                     | 50.27                    | 19                    | 20.25                 | 8.30         |
| 23       | 74                | 85                     | 81                | 84                     | 71                     | 46.99                    | 61                    | 19.15                 | 2.39         |
| 24       | 59                | 66                     | 57                | 59                     | 36                     | 78.20                    | 1                     | 4.54                  | 8.66         |
| 25       | 47                | 43                     | 28                | 47                     | 28                     | 50.00                    | 16                    | 19.07                 | 22.52        |
| 26       | 72                | 58                     | 51                | 69                     | 51                     | 64.61                    | 27                    | 12.92                 | 30.12        |
| 27       | 45                | 62                     | 32                | 61                     | 34                     | 73.09                    | 17                    | 22.37                 | 23.61        |
| 28       | 73                | 69                     | 60                | 80                     | 54                     | 86.14                    | 13                    | 24.00                 | 27.42        |
| 29       | 74                | 69                     | 81                | 84                     | 86                     | 77.66                    | 6                     | 27.66                 | 40.68        |
| 30       | 85                | 85                     | 71                | 89                     | 69                     | 92.96                    | 5                     | 30.53                 | 56.08        |
| Average  | <b>63.18</b>      | 66.51                  | 56.81             | <b>67.5</b>            | 24.6                   | <b>69.53</b>             | 17.84                 | 19.26                 | <b>20.53</b> |
| Time (s) | 13.5              | 4.7                    | 2.3               | 21.5                   | 1.8                    | 0.6                      | 4.4                   | 0.1                   | 0.2          |



Figure 6: Qualitative 6D Object Detection results on T-LESS Primesense scenes. Only 18 of 30 objects are used to train the Multi-Path encoder. Left: Predictions of the RGB-based pipeline; Middle-left: Error in depth [mm]; Middle-right: ICP-refined results; Right: Refined error in depth [mm]. Note that only one instance per class is predicted following the BOP [18] rules.